J. Appl. Comput. Mech., xx(x) (2026) 1-12
DOI: 10.22055/jacm.2026.49533.6054

ISSN: 2383-4536
jacm.scu.ac.ir

Shahid Chamran
University of Ahvaz

Journal of
Applied and Computational Mechanics

Research Paper

Shear-thinning Control of Transition and Turbulent Dissipation: A Generalised Newtonian Spectral Study

Ashish Gad

Department of Mechanical Engineering, The Engineering College, Monk Ferry, Birkenhead, CH41 5LH, United Kingdom, Email: ashishgad.mech@gmail.com

Received July 03 2026; Revised August 17 2026; Accepted for publication September 11 2026.
✉ Corresponding author: A. Gad (ashishgad.mech@gmail.com)

Abstract. This research investigates how shear-dependent viscosity affects the transition to turbulence and fully developed turbulent statistics in an inelastic, generalised Newtonian fluid governed by the Carreau-Yasuda model. To facilitate this, a pseudo-spectral solver for the two-dimensional incompressible Navier-Stokes equations was developed. By evaluating the variable-viscosity diffusion term through the divergence of the deviatoric stress, the solver exactly recovers the Newtonian limit. The method was rigorously verified against standard analytical benchmarks, achieving high precision. The study demonstrates that in a perturbed free shear layer, shear-thinning suppresses perturbation kinetic energy amplification by up to three orders of magnitude compared to a Newtonian baseline. This reduction affects both linear growth and saturation levels, becoming more pronounced at higher Reynolds numbers. In steady forced turbulence, reduced viscosity in high-strain areas sharpens the small-scale vorticity field. This shifts energy to higher wavenumbers and raises the mean enstrophy by roughly eighteen per cent. Because viscosity drops exactly where strain peaks, the dissipation field becomes significantly less intermittent. Furthermore, a dissipation-reduction metric decreases steadily as the power-law index falls, by up to about 83 per cent at an index of 0.4. While the reduction of viscosity in high-strain regions is a direct property of the shear-thinning model, the new understanding obtained here lies in its net effect on the turbulent structure: the small-scale vorticity and the dissipation field respond in opposite directions, the former becoming finer while the latter becomes smoother. The work thus provides verifiable insight for ongoing investigations into wall-bounded generalised Newtonian flow and elasto-inertial turbulence.

Keywords: Shear-thinning fluid; Generalised Newtonian fluid; Carreau–Yasuda model; Pseudo-spectral method; Transition to turbulence.

1. Introduction

Many fluids of industrial and biological importance, including polymer solutions, slurries, paints, drilling muds and blood, possess a viscosity that depends on the local rate of strain rather than remaining constant. For a large and practically important subclass, the generalised Newtonian fluids, the apparent viscosity is well represented as a function of the scalar shear rate alone, with elastic effects either absent or negligible within the relevant range of concentration and deformation rate [1, 2]. The most common behaviour is shear-thinning, in which viscosity decreases with increasing shear rate. Understanding how such rheology alters the transition to turbulence and the structure of fully developed turbulence is central to the prediction of pressure losses and mixing in these systems.

A consistent picture has emerged from direct numerical simulation (DNS) of wall-bounded generalised Newtonian turbulence. Rudman and co-workers established spectral-element DNS of turbulent pipe flow of shear-thinning fluids and documented the weakening of near-wall turbulence and the resulting modification of the friction factor [3-6]. In channel geometry, Arosemena et al. [7] reported turbulence statistics for generalised Newtonian fluids at low Reynolds number, and Arosemena et al. [8] showed that shear-thinning causes the quasi-streamwise vortices to grow in size, lift away from the wall and weaken in intensity. Karahan et al. [9] extended these observations to power-law and Herschel–Bulkley fluids, finding that shear-thinning and yield stress both weaken turbulence and promote strong anisotropy, with the dominant effects confined to the inner layer.

Whether purely inelastic shear-thinning produces genuine drag reduction remains subtle. Several wall-bounded studies report a reduced wall shear stress and a thinning of the viscous sublayer, yet the magnitude of any net drag reduction depends sensitively on the choice of viscosity scale used to define the Reynolds number, and recent work emphasises that the inelastic contribution is modest compared with the elastic mechanism operating in dilute polymer solutions [6, 8]. This motivates careful, controlled comparisons in which the rheology is varied systematically while all other parameters are held fixed.

The present work contributes such a controlled comparison using a deliberately economical two-dimensional pseudo-spectral model. The aim is not to reproduce three-dimensional wall turbulence quantitatively but to isolate, at low cost and with full

Published online: September 19 2026

analytical verifiability, the mechanism by which a strain-dependent viscosity reshapes transition and the small-scale structure of turbulence. The vorticity–streamfunction formulation eliminates the pressure and enforces incompressibility identically, and the spectral discretisation provides exponential accuracy that permits unambiguous verification against closed-form solutions. Within this framework we examine three questions: how shear-thinning modifies the growth of disturbances in a free shear layer; how it alters the energy spectrum, the velocity-fluctuation statistics and the spatial organisation of dissipation in statistically steady turbulence; and how a dissipation-reduction metric, defined below and distinct from wall-friction drag, varies with the power-law index. The two-dimensional idealisation and its consequences, in particular the dominance of an enstrophy cascade rather than a three-dimensional energy cascade [10], are discussed openly in the relevant section. Because two-dimensional and three-dimensional turbulence differ fundamentally in their cascade dynamics, the two-dimensional model adopted here having an inverse energy cascade and a direct enstrophy cascade rather than the three-dimensional energy cascade, the quantitative measures of dissipation and drag reported below are to be read as properties of this idealised model, and are interpreted throughout as indicative trends rather than transferable predictions for three-dimensional or wall-bounded flow.

2. Governing Equations and Constitutive Model

2.1. Balance laws

We consider an incompressible fluid of constant mass density ρ occupying a region of R^2 for the time-dependent calculations and a planar channel $-1 \le y \le 1$ for the laminar benchmarks. The balances of mass and linear momentum, in the absence of body forces, reduce to:

$$\nabla \cdot \mathbf{u} = 0, \qquad \rho(\partial_t \mathbf{u} + \mathbf{u} \cdot \nabla \mathbf{u}) = -\nabla p + \nabla \cdot \boldsymbol{\tau}, \tag{1}$$

where $\mathbf{u} = (u, v)$ is the velocity, p the pressure and τ the deviatoric stress. In the two-dimensional flows considered here the vorticity has only an out-of-plane component, so we work with the scalar $\omega = \partial_x v - \partial_y u$.

2.2. Rate of strain and the scalar shear rate

For a generalised Newtonian fluid, the deviatoric stress is co-linear with the rate-of-strain tensor, with a scalar apparent viscosity depending only on the second invariant of S [1, 2]:

$$\boldsymbol{\tau} = 2\mu(\dot\gamma)\,\mathbf{S}, \qquad \mathbf{S} = ½(\boldsymbol{\nabla}\mathbf{u} + \boldsymbol{\nabla}\mathbf{u}^{\mathrm{T}}), \qquad \dot\gamma = \sqrt{2\,\mathbf{S}\!:\!\mathbf{S}} \tag{2}$$

The factor $\frac{1}{2}$ in S is the standard definition that makes S the symmetric part of the velocity-gradient tensor ∇u, so that S is symmetric ($S_{ij} = S_{ji}$) and its trace $S_{ii} = \nabla \cdot \mathbf{u}$ vanishes for an incompressible flow. Its consistency with the conventional shear rate is shown by the canonical simple shear flow $\mathbf{u} = (\dot\gamma_0 y,\, 0)$, for which the only non-zero velocity gradient is $\partial_y u = \dot\gamma_0$.

The rate-of-strain tensor is then:

$$\mathbf{S} = \frac{1}{2}(\nabla\mathbf{u} + \nabla\mathbf{u}^{\mathrm{T}}) = \begin{pmatrix} 0 & \frac{1}{2}\dot\gamma_0 \\ \frac{1}{2}\dot\gamma_0 & 0 \end{pmatrix},$$

So that, $\mathbf{S}\!:\!\mathbf{S} = 2(\frac{1}{2}\dot\gamma_0)^2 = \frac{1}{2}\dot\gamma_0^2$ and the scalar shear rate is:

$$\dot\gamma = \sqrt{2\,\mathbf{S}\!:\!\mathbf{S}} = \sqrt{2 \cdot \frac{1}{2}\dot\gamma_0^2} = \dot\gamma_0.$$

The factor $\frac{1}{2}$ in S and the factor 2 under the square root in γ are therefore paired so that γ reduces exactly to the imposed shear rate $\dot\gamma_0$ in simple shear, recovering the standard rheological definition against which the Carreau--Yasuda viscosity is calibrated.

In two dimensions, under incompressibility $Sxx + Syy = 0$, the scalar shear rate simplifies to:

$$\dot\gamma = \sqrt{4(\partial_x u)^2 + (\partial_y u + \partial_x v)^2}. \tag{3}$$

Hence $\dot\gamma$ grows with both the local streamwise strain rate and the local shear, and the viscosity is set by the instantaneous local straining alone, with no memory of past deformation. This is the defining property of the inelastic class of constitutive models.

2.3. The generalised Newtonian framework

Generalised Newtonian models neglect elasticity altogether and treat the fluid as having a viscosity that is a deterministic, scalar-valued function of the current local shear rate. Operationally, only the local instantaneous value of $\dot\gamma$ enters the diffusion operator, so the cost of evaluating the constitutive law is that of a single pointwise function evaluation: no additional fields, no history variables, and no viscoelastic coupling terms need be transported or stored. This is the principal computational advantage of the class in a spectral framework. The choice of an inelastic law is a deliberate restriction; the leading-order inelastic mechanism in a two-dimensional incompressible flow is exactly the response to shear-dependent viscosity that we isolate here, the same mechanism identified in recent DNS as the inelastic contribution to drag reduction in shear-thinning turbulent flow [6-9].

2.4. The Carreau-Yasuda model

We adopt the Carreau–Yasuda constitutive equation for the apparent viscosity [11, 12]. The model is widely used for computational studies of shear-thinning flow and heat transfer [31]:

$$\mu(\dot\gamma) = \mu_\infty + (\mu_0 - \mu_\infty)[1 + (\lambda\dot\gamma)^a]^{(n-1)/a}. \tag{4}$$

Here μ_0 and μ_∞ are the zero-shear and infinite-shear viscosities, λ a relaxation time, n the power-law index ($n = 1$ Newtonian, $n < 1$ shear-thinning) and a the Yasuda parameter controlling the width of the transition between the two plateaux; $a = 2$ recovers the Carreau model. In the limit $\lambda\dot\gamma \to \infty$ with $\mu_\infty = 0$ the model reduces to the Ostwald–de Waele power law $\mu = K\dot\gamma^{n-1}$ with $K = \mu_0\lambda^{n-1}$, the limit in which the laminar channel profile admits the exact analytical form used as a verification benchmark in section 4.2.

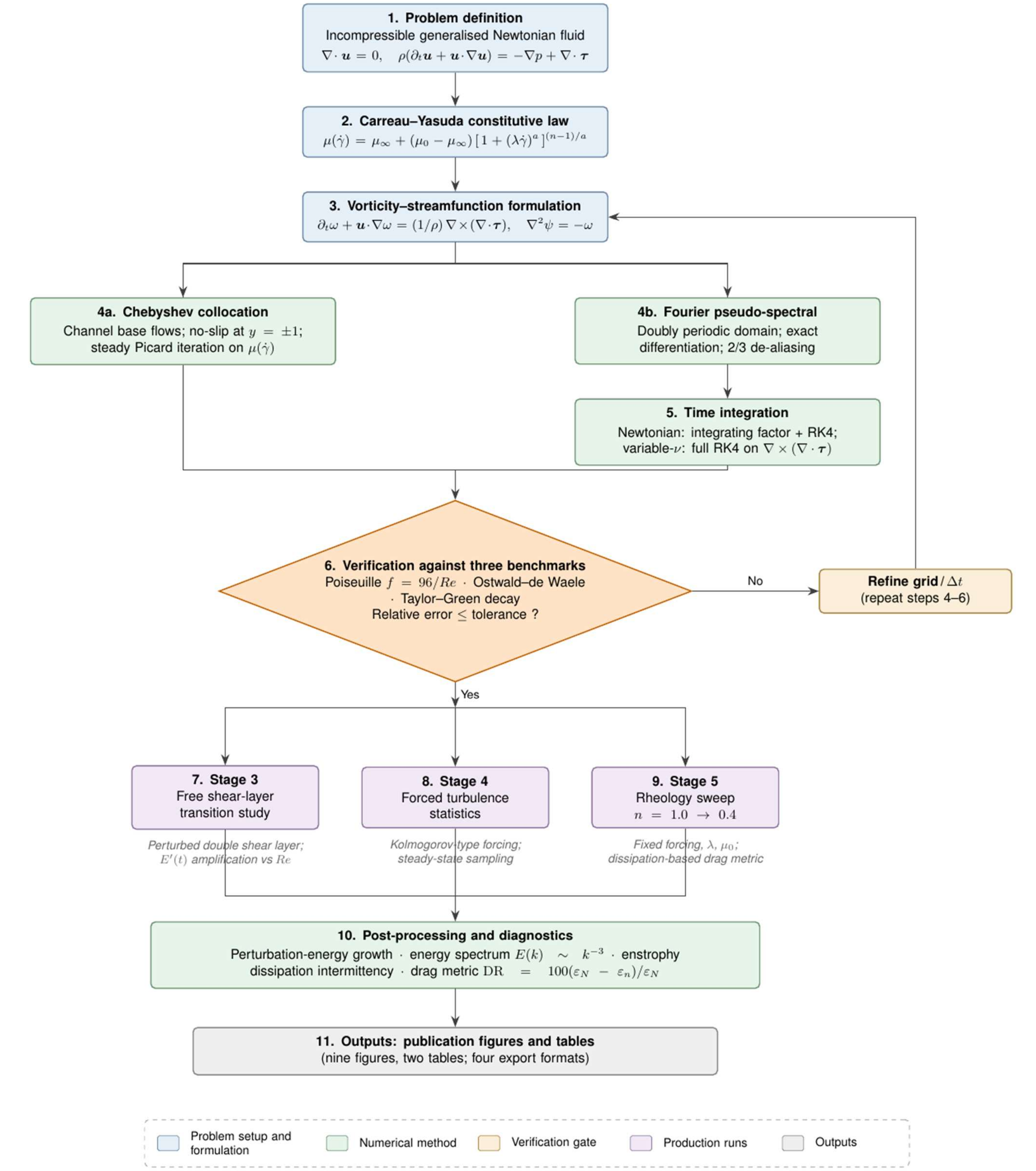

Fig. 1. Process flowchart of the simulation pipeline, from the governing equations and constitutive model through discretisation, verification against three analytical benchmarks, the three production runs and the post-processing diagnostics.

2.5. Vorticity-streamfunction formulation

Introducing the streamfunction ψ with $u=\partial_y\psi$ and $v=-\partial_x\psi$ satisfies continuity identically. Taking the curl of the momentum equation removes the pressure and yields:

$$\partial_t\omega+\mathbf{u}\cdot\nabla\omega=\frac{1}{\rho}\,\nabla\times(\nabla\cdot\boldsymbol{\tau}),\qquad \nabla^2\psi=-\omega. \tag{5}$$

when μ is uniform the curl of the viscous term reduces to $\mu\nabla^2\omega/\rho$. The stress-divergence form on the right is its exact generalisation to variable viscosity and is the form implemented in section 3.

2.6. Non-dimensionalisation and Reynolds number

The Reynolds number is built from the zero-shear kinematic viscosity $\nu_0 = \mu_0/\rho$ and the scales appropriate to each configuration. Using the zero-shear viscosity throughout makes the Newtonian limit a clean reference point, matching the convention of the wall-bounded DNS literature [7-9]. The local Reynolds number experienced by the flow is set by the local apparent viscosity and therefore varies in space and time; this is quantified in section 5.3 through the volume-averaged ratio ν_{eff}/ν_0. Time is made nondimensional throughout by the advective time scale appropriate to each configuration: for the free shear layer this is $t_c = \delta/\Delta U$, one shear-layer turnover; for the forced turbulence it is the large-eddy turnover time, against which the averaging window of the statistics is many units long. Unless stated otherwise, all times reported in the figures are in these units.

3. Numerical Method

The solver targets the vorticity–streamfunction system and is organised around a single state advanced in time. The overall structure of the solver and the sequence of verification and production runs are summarised in Fig. 1. Two spatial discretisations are used, selected by geometry; the time-integration scheme is selected by the rheology. Representative code excerpts are given to make the implementation reproducible; they are lightly abridged from the working solver.

3.1. Spatial discretisation

3.1.1. Chebyshev collocation for the channel base flows

For the laminar base flows the wall-normal coordinate is discretised at the Gauss-Lobatto points $y_j = \cos(j\pi/N)$, $j = 0, \ldots, N$, which place nodes exactly on the walls and so enforce the no-slip condition naturally [13, 14]. The steady, nonlinear boundary-value problem $\mathrm{d}/\mathrm{d}y\,[\mu(|\mathrm{d}u/\mathrm{d}y|)\,\mathrm{d}u/\mathrm{d}y] = -G$, with G the imposed pressure gradient and no-slip walls, is solved by Picard iteration: the apparent viscosity is frozen at the current velocity iterate, the resulting linear variable-coefficient operator is assembled from the collocation derivative matrix and inverted subject to the boundary rows, and the velocity is updated under-relaxed until the change between successive iterates falls below 10^{-12}. The full routine is listed in Appendix A (Listing A.1).

3.1.2. Fourier pseudo-spectral method for the periodic domain

The time-dependent flows are solved on a doubly periodic square with $N \times N$ modes. Spatial derivatives are evaluated exactly in Fourier space by multiplication with the wavenumber, nonlinear products are formed in physical space by fast Fourier transform, and the quadratic advection term is de-aliased by the two-thirds rule [15]. The streamfunction is recovered from the vorticity by solving the Poisson equation $\nabla^2\psi = -\omega$ spectrally, that is by dividing the transformed vorticity by the squared wavenumber magnitude (with the mean mode set to zero), and the velocity follows as $\mathbf{u} = (\partial_y\psi, -\partial_x\psi)$. The construction of the spectral operators and the velocity recovery is listed in Appendix A (Listing A.2).

3.1.3. Variable-viscosity diffusion in stress-divergence form

The variable-viscosity term is evaluated as $\nabla \times (\nabla \cdot \boldsymbol{\tau})$ with $\boldsymbol{\tau} = 2\mu(\dot{\gamma})\mathbf{S}$, following the steps summarised in Algorithm 1. The velocity-gradient components are formed spectrally and combined into the scalar shear rate; the apparent viscosity is evaluated pointwise through the constitutive law; the deviatoric-stress components are assembled in physical space; and the divergence and curl are taken spectrally to give the vorticity tendency. The routine is exact in the Newtonian limit: when μ is constant it collapses to $-\nu_0 k^2\hat{\omega}$, recovering the constant-property solver identically rather than approximately, a property confirmed numerically to a relative error of 4×10^{-12}. The full routine is listed in Appendix A (Listing A.3).

Algorithm 1: Variable-viscosity diffusion (vorticity tendency):

```
Require: spectral vorticity ω̂
1: if fluid is Newtonian then return −ν₀k²ω̂ ▸ exact constant-viscosity limit
2: recover u = (u, v) from ω̂ via the streamfunction
3: form velocity gradients ∂ₓu, ∂ᵧu, ∂ₓv, ∂ᵧv spectrally
4: γ̇ ← √(2(∂ₓu)² + 2(∂ᵧv)² + (∂ᵧu + ∂ₓv)²)
5: ν ← ν(γ) ▸ Carreau–Yasuda, evaluated pointwise
6: assemble stress τ₁₁ = 2ν∂ₓu, τ₂₂ = 2ν∂ᵧv, τ₁₂ = ν(∂ᵧu + ∂ₓv)
7: f ← ∇·τ (spectrally)
8: return [∇ × f], de-aliased by the two-thirds mask
```

3.2. Time integration

In the Newtonian case the diffusion term is linear and diagonal in Fourier space and is integrated exactly by an integrating factor, while the nonlinear advection is advanced with the classical fourth-order Runge–Kutta scheme. When the viscosity varies in space the diffusion operator is no longer diagonal, so the full right-hand side, comprising the nonlinear advection, the variable-viscosity term of Algorithm 1, the large-scale drag and the steady forcing, is advanced with the same fourth-order Runge–Kutta scheme. The time step is set by the most restrictive of the advective Courant–Friedrichs–Lewy limit, the explicit diffusive limit and the sharpest resolvable Fourier mode. Because the effective viscosity in strongly shear-thinning cases is well below ν_0, the diffusive constraints are eased relative to the Newtonian limit. The assembly of the forced right-hand side is listed in Appendix A (Listing A.4).

Table 1. Discretisation parameters and convergence settings for each configuration.

Configuration	Grid	Δt	Re	T
Plane Poiseuille	Cheb. N = 33	steady	≤ 10^4	–
Power-law channel	Cheb. N = 65	steady	≤ 10^4	–
Taylor–Green	128^2	5×10^{-4}	10^2	10
Free shear layer	256^2	2×10^{-3}	10^2 – 10^4	30
Forced turbulence	512^2	5×10^{-3}	10^3	200
Rheology sweep	512^2	5×10^{-3}	10^3	1000

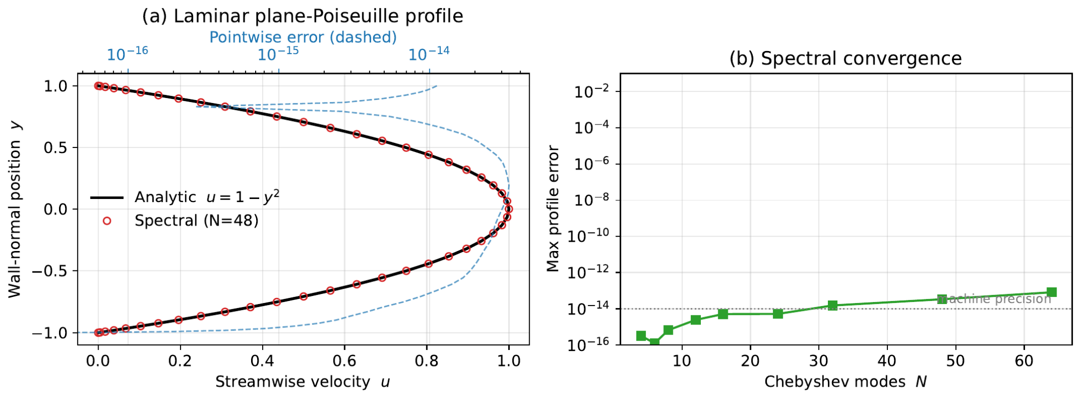

Fig. 2. Verification of the Newtonian laminar solver (Chebyshev collocation, $N = 33$ modes); All quantities are nondimensional, (a) Spectral solution (symbols) against the analytical parabola $u(y) = 1 - y^2$ (line), with the pointwise error on the upper axis, (b) Maximum profile error against the number of Chebyshev modes, showing convergence to machine precision.

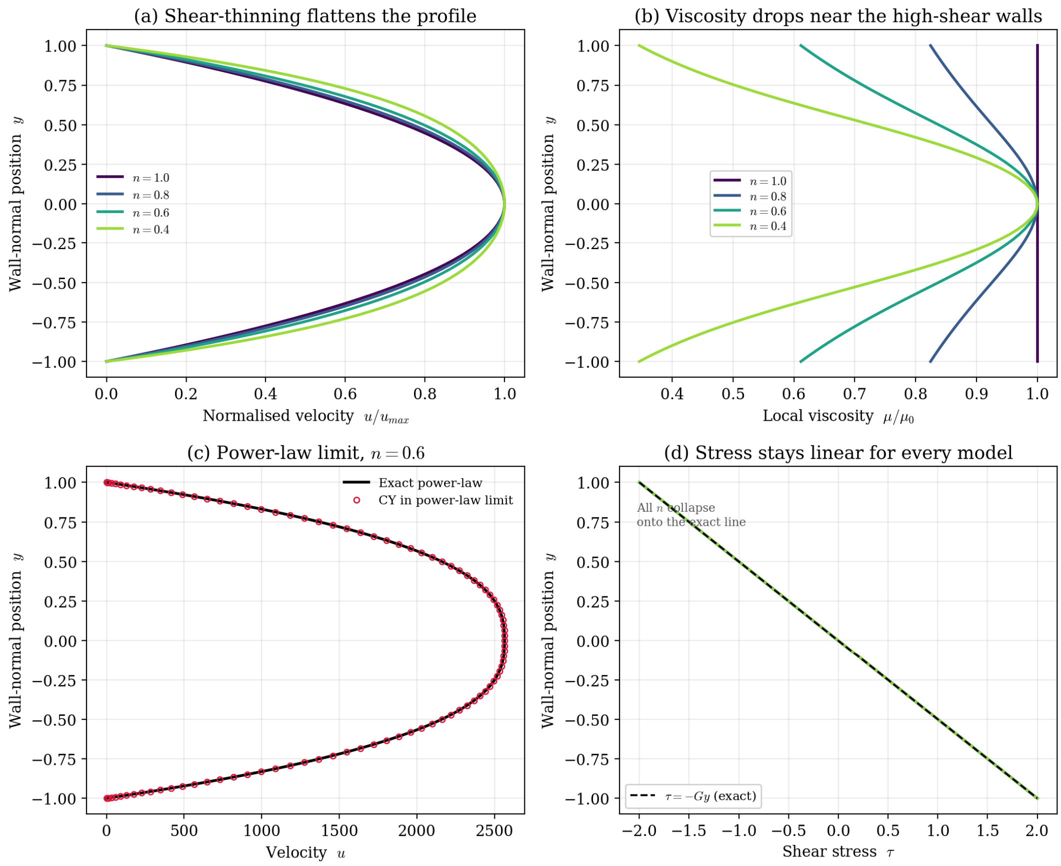

Fig. 3. Carreau–Yasuda laminar channel verification (Chebyshev collocation, $N = 65$, Yasuda parameter $a = 2$); All quantities are nondimensional; (a) Velocity profiles normalised by centreline velocity for decreasing power-law index $n = 1.0, 0.8, 0.6, 0.4$, (b) Corresponding apparent-viscosity profiles, (c) Power-law limit against the exact Ostwald–de Waele solution, (d) Shear-stress linearity, a model-independent identity satisfied by all rheologies.

3.3. Numerical parameters and convergence

Table 1 lists the discretisation parameters. For every case the resolution was doubled and the time step halved, and the relevant diagnostic was confirmed unchanged to within the relative error quoted in the corresponding verification section.

4. Verification

The solver is verified against three analytical benchmarks. All errors quoted are relative to the closed-form result.

4.1. Laminar plane-Poiseuille flow

For a Newtonian fluid driven by a constant pressure gradient between no-slip walls at $y = \pm 1$ the profile is the parabola $u(y) = 1 - y^2$. The Chebyshev solver reproduces this to a maximum pointwise error of order 10^{-14} across grid refinement (Figs. 2(a), 2(b)). The Darcy friction factor agrees with the exact relation $f = 96/ReDh$, based on the hydraulic diameter $Dh = 2H$, to a relative error of 2×10^{-14}, verified independently through the imposed pressure gradient and the resolved wall shear stress.

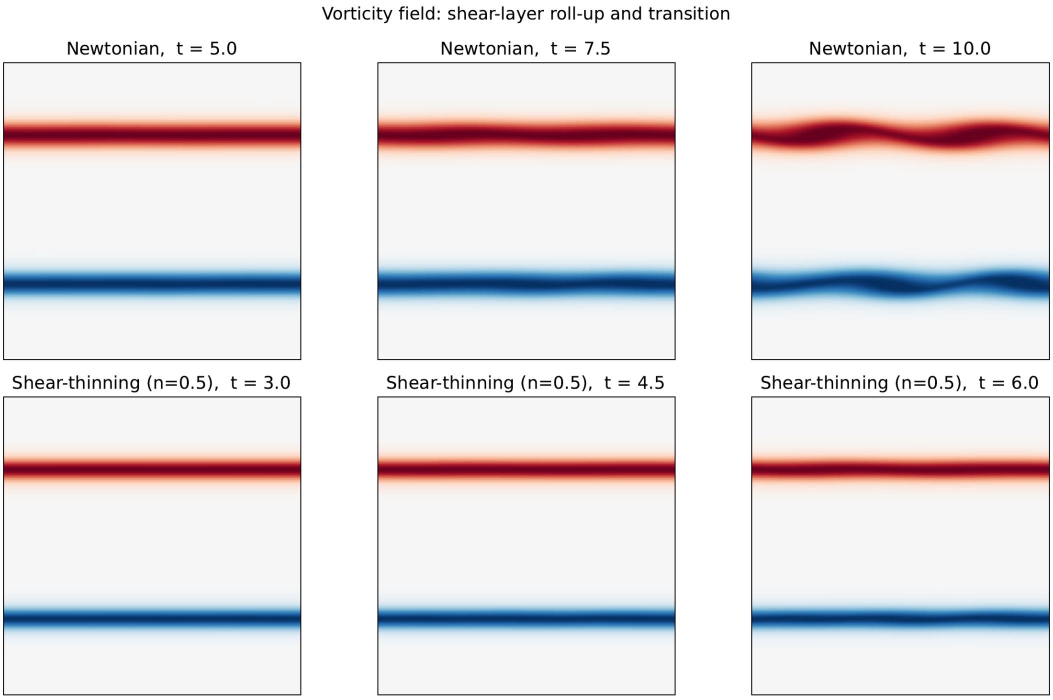

Fig. 4. Vorticity field during shear-layer roll-up for the Newtonian fluid (top) and the shear-thinning fluid with $n = 0.5$ (bottom), at matched Reynolds number $Re_\delta = 160$ and Yasuda parameter $a = 2$, shown at nondimensional time $t/t_c = 6$ (with $t_c = \delta/\Delta U$); Vorticity is nondimensional.

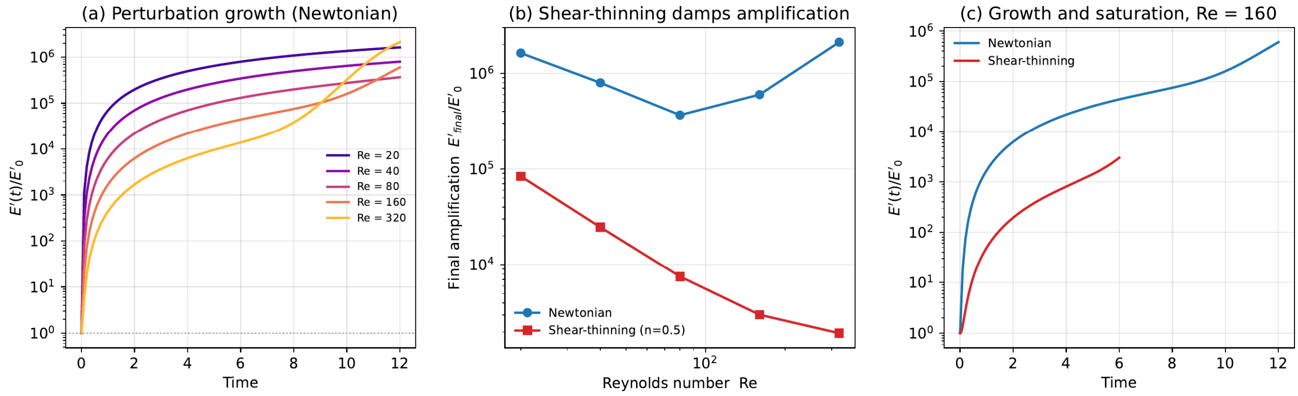

Fig. 5. Transition diagnostics for the perturbed free shear layer (grid 256², Yasuda parameter $a = 2$). Time is nondimensional, in units of the advective time scale $t_c = \delta/\Delta U$ (δ the layer thickness, ΔU the velocity difference; one unit is one shear-layer turnover);
(a) Growth of the normalised perturbation energy $E'(t)/E'(0)$ for the Newtonian fluid across Reynolds number $Re_\delta = \Delta U\delta/\nu_0 = 20 - 320$,
(b) Final amplification $E'_{final}/E'(0)$ against Re_δ for the Newtonian and shear-thinning ($n = 0.5$) fluids,
(c) Time histories of the perturbation energy at fixed $Re_\delta = 160$, comparing the two fluids.

4.2. Power-law and stress-linearity benchmarks

With the Carreau–Yasuda parameters driven towards the power-law limit, the computed profile matches the exact Ostwald–de Waele solution to a relative L_2 error of order 10^{-7} (Fig. 3(c)). A model-independent check is provided by the requirement that, for fully developed channel flow of any generalised Newtonian fluid, the total shear stress varies linearly across the gap, $\tau(y) = -Gy$, irrespective of the viscosity law. This identity is satisfied to between 10^{-13} and 10^{-10} for every rheology tested (Fig. 3(d)). For strongly shear-thinning fluids the power-law profile develops a slope cusp at the centreline, and a global Chebyshev basis then shows a localised Gibbs oscillation there; the error is concentrated at $y = 0$ and decays away from it, an expected property of spectral approximation of non-smooth solutions.

4.3. Taylor-Green vortex

The decaying Taylor–Green vortex provides an exact unsteady solution, with vorticity decaying as $exp(-2k^2\nu t)$. The solver reproduces both the decay rate and the spatial structure to a relative error of order 10^{-14}, confirming the advective and diffusive operators and the de-aliasing.

5. Results

5.1. Transition in a free shear layer

Transition is studied in a periodic double shear layer perturbed by a small divergence-free disturbance, with the Reynolds number based on the shear velocity and layer thickness. Figure 4 shows the vorticity field for both fluids at matched conditions. The Newtonian layer develops the familiar Kelvin–Helmholtz waviness, whereas the shear-thinning layer remains comparatively flat over the same interval. The mechanism is direct: in the high-strain braid regions the apparent viscosity drops, but the accompanying redistribution of base-flow vorticity thickens the effective shear-layer profile and lowers its peak strain, reducing the growth rate of the inflectional instability that drives roll-up.

The perturbation kinetic energy $E'(t)$ grows and saturates in all cases, consistent with the inviscid instability of this base flow; the meaningful comparison is the degree of amplification rather than a critical Reynolds number. For the Newtonian fluid the final amplification $E' final/E'(0)$ lies between roughly 4×10^5 and 2×10^6 across $Re = 20$ to 320, whereas the shear-thinning fluid is held to between about 2×10^3 and 8×10^4, a suppression of one to three orders of magnitude. Two features of Fig. 5 deserve emphasis. First, the initial exponential growth rate is itself reduced by shear-thinning, not merely the saturation level: the shear-thinning curves rise more slowly from the outset, indicating that the rheology damps the linear instability and not only its nonlinear development. Second, the suppression strengthens with Reynolds number, so the two curves in Fig. 5(b) diverge as Re increases. This is the signature of the underlying mechanism: at higher Reynolds number the disturbance enstrophy is produced in ever-thinner, higher-strain layers, exactly where the apparent viscosity is most strongly reduced. The behaviour is consistent with the wall-bounded weakening of turbulence-producing structures [8, 9] and with experimental reports of delayed transition in shear-thinning pipe flow [16].

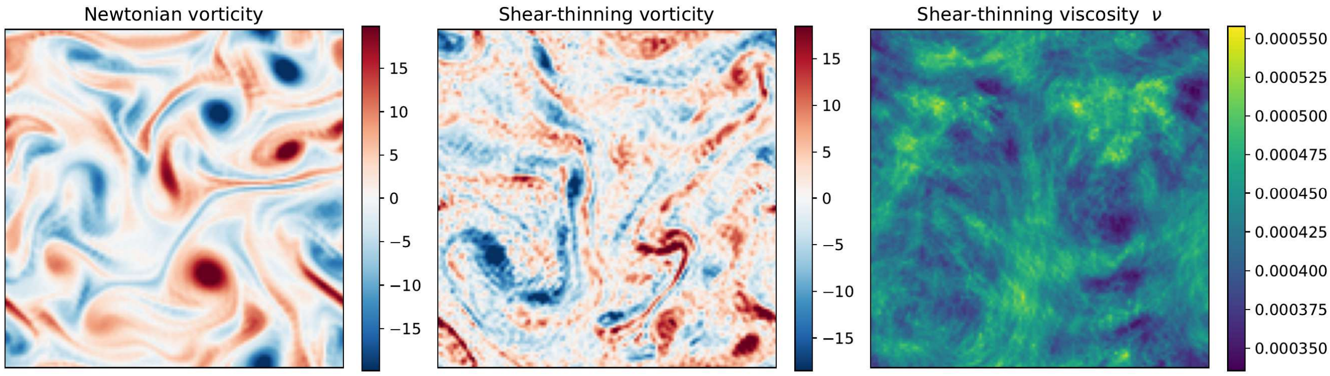

Fig. 6. Developed turbulence fields at zero-shear Reynolds number $Re = 10^3$, forcing wavenumber $k_f = 4$, on a 512^2 grid; shear-thinning case $n = 0.5$, $a = 2$. Fields are nondimensional and shown at a representative instant in the statistically steady state; Newtonian vorticity (left), shear-thinning vorticity (centre) and the shear-thinning apparent-viscosity field $\nu(\dot\gamma)/\nu_0$ (right).

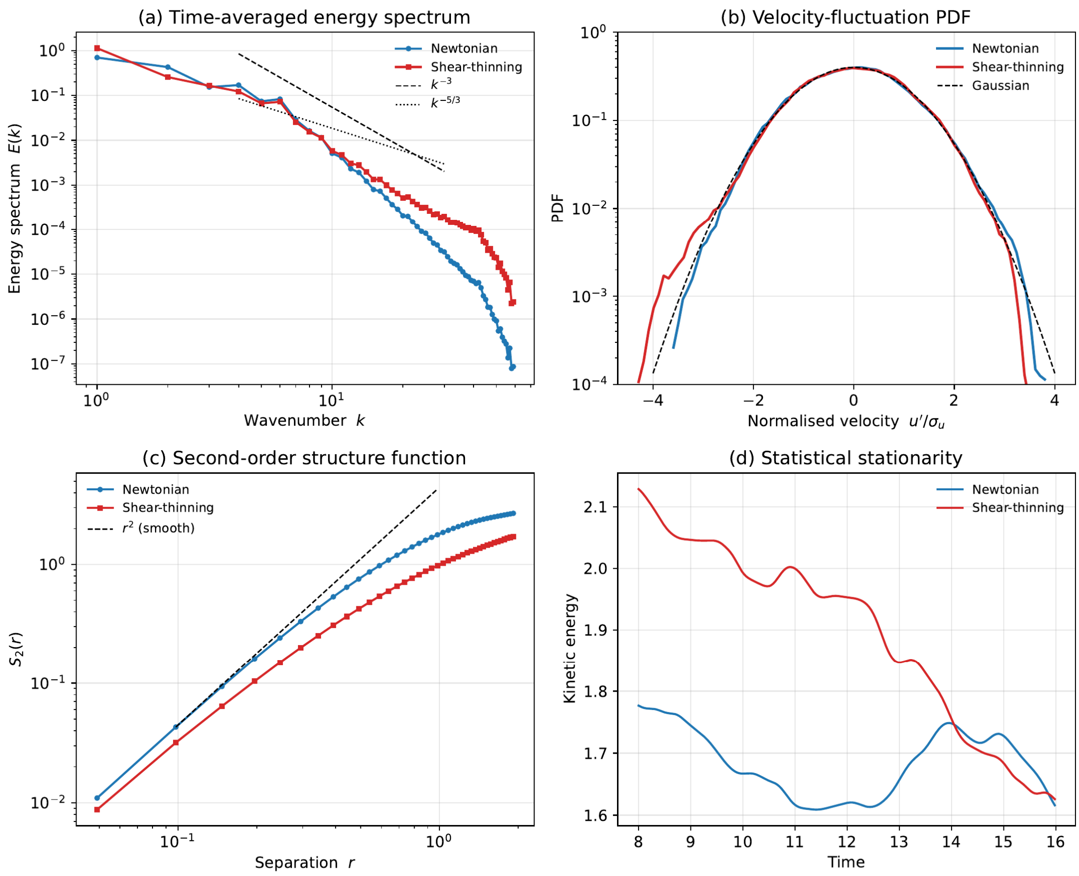

Fig. 7. Turbulence statistics for the Newtonian and shear-thinning ($n = 0.5, a = 2$) fluids at $Re = 10^3$, $k_f = 4$, time-averaged over an interval of about 100 large-eddy turnover times in the statistically steady state. All quantities are nondimensional; (a) Time-averaged energy spectrum $E(k)$, with k^{-3} and $k^{-5/3}$ references; least-squares slopes over $4 \le k \le 20$ are about -4.3 (Newtonian) and -3.6 (shear-thinning), (b) Velocity-fluctuation probability density, normalised by the standard deviation, against a Gaussian, (c) Second-order structure function, showing r^2 scaling at small separation, (d) Kinetic-energy time series confirming statistical stationarity over the averaging window.

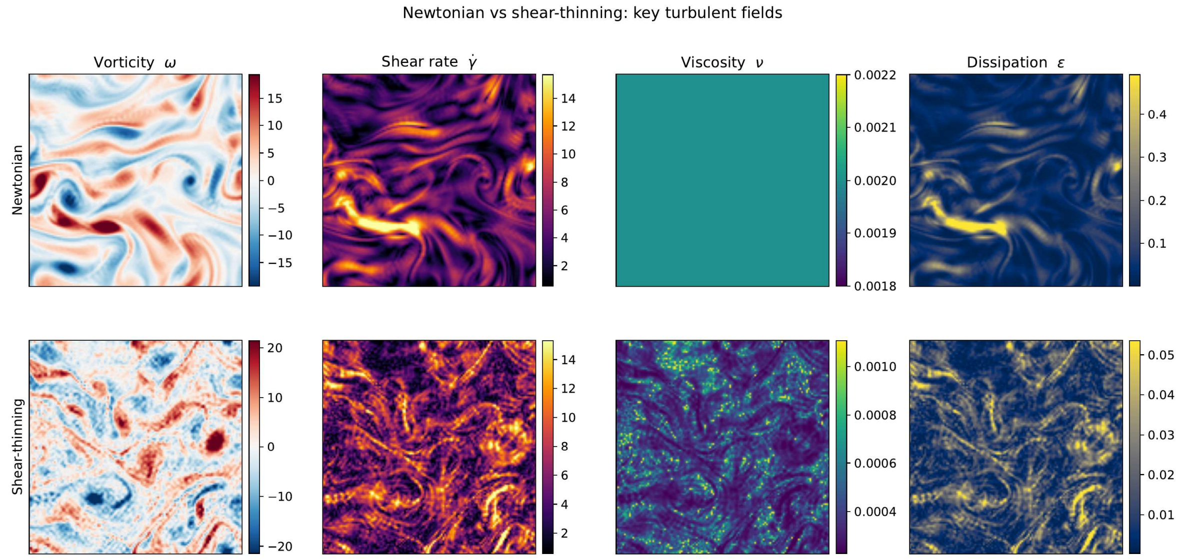

Fig. 8. Newtonian (top) and shear-thinning (bottom, $n = 0.5, a = 2$) turbulent fields at $Re = 10^3$, $k_f = 4$, at a representative instant in the statistically steady state; all fields nondimensional. Columns: vorticity ω, scalar shear rate $\dot{\gamma}$, apparent viscosity $\nu(\dot{\gamma})/\nu_0$, and viscous dissipation $\varepsilon = \nu\dot{\gamma}^2$. The apparent-viscosity field is the pointwise image of the shear-rate field through the constitutive law; shear-thinning sharpens the vorticity while making the dissipation less intermittent (coefficient of variation $1.3 \to 0.8$).

5.2. Fully developed turbulence

Statistically steady turbulence is generated by a fixed Kolmogorov-type forcing with a weak large-scale drag. Figure 6 contrasts the developed fields. The Newtonian vorticity field is organised into coherent vortices and smooth filaments; the shear-thinning field is visibly finer-grained. The viscosity field is uniform for the Newtonian fluid by construction and strongly modulated for the shear-thinning fluid, falling in the high-strain filaments. The mean enstrophy is correspondingly higher for the shear-thinning fluid, by approximately eighteen per cent (22.4 against 18.9 in the present non-dimensionalisation), and its mean kinetic energy is also slightly larger (1.89 against 1.68), both consequences of reduced small-scale dissipation.

Figure 7 reports the turbulence statistics. The time-averaged energy spectrum follows the steep fall-off characteristic of the two-dimensional enstrophy cascade [10], whose dimensional prediction is a k^{-3} range. A least-squares fit over $4 \leq k \leq 20$ gives a slope of about -4.3 for the Newtonian fluid and a distinctly shallower -3.6 for the shear-thinning fluid; the shift towards the -3 reference under shear-thinning is the spectral signature of energy surviving to smaller scales. Quantitatively, the fraction of energy held above $k = 15$ is about 0.49 per cent for the shear-thinning fluid against 0.19 per cent for the Newtonian fluid, an increase by a factor of roughly 2.6. The velocity-fluctuation probability density remains close to Gaussian in both cases (Fig. 7(b)); the shear-thinning distribution acquires a small negative skewness, about -0.08, and a mild positive excess kurtosis, about +0.06, a weak intermittency consistent with the larger population of energetic small scales. The second-order structure function follows the smooth-field r^2 scaling at small separation (Fig. 7(c)), and the kinetic-energy time series confirm statistical stationarity (Fig. 7(d)).

The extended field atlas of Fig. 8 makes the mechanism explicit. The apparent-viscosity field is the pointwise image of the shear-rate field through the constitutive law, lowest precisely where the strain is highest; across the shear-thinning field the local viscosity ranges over an order of magnitude, from about 0.09 to 1.0 of the zero-shear value, with a spatial mean near 0.21. A noteworthy and perhaps counterintuitive consequence concerns the dissipation field. Although the shear-thinning vorticity is visibly finer-grained, its dissipation is markedly *less* intermittent than the Newtonian one: the coefficient of variation of the local dissipation falls from 1.3 to 0.8, and the share of total dissipation concentrated in the most intense five per cent of the area falls from 27 to 16 per cent. The reason is intrinsic to the constitutive law. Because the dissipation density is $\varepsilon = \nu(\dot{\gamma})\dot{\gamma}^2$ and the viscosity decreases where the strain is largest, shear-thinning acts as a self-limiter on the dissipation, capping the extreme events that dominate the Newtonian field. The fine scales in the vorticity and the smoothness of the dissipation are two faces of the same mechanism: energy reaches smaller scales because viscosity is locally suppressed, and the dissipation there is held in check by that same suppression.

5.3. Dissipation and the effect of the power-law index

To quantify the rheological effect, we vary the power-law index from 1.0 to 0.4 at fixed forcing, relaxation time and zero-shear viscosity, and record a dissipation-reduction metric, defined as the fractional decrease of the volume-averaged viscous dissipation relative to the Newtonian reference:

$$\mathrm{DR}(\%) = 100\,\frac{\varepsilon_N - \varepsilon_n}{\varepsilon_N}, \qquad \varepsilon = \langle\, \nu(\dot{\gamma})\dot{\gamma}^2\, \rangle, \tag{6}$$

Table 2. Effect of the power-law index on the volume-averaged apparent viscosity and the dissipation-reduction metric, with marginal increment per 0.1 decrement in *n*.

n	ν_{eff}/ν_0	DR (%)	Increment (pp)
1.0	1.000	0.0	–
0.9	0.726	31.7	31.7
0.8	0.531	53.0	21.2
0.7	0.383	65.3	12.4
0.6	0.271	71.9	6.6
0.5	0.194	79.3	7.4
0.4	0.129	82.8	3.5

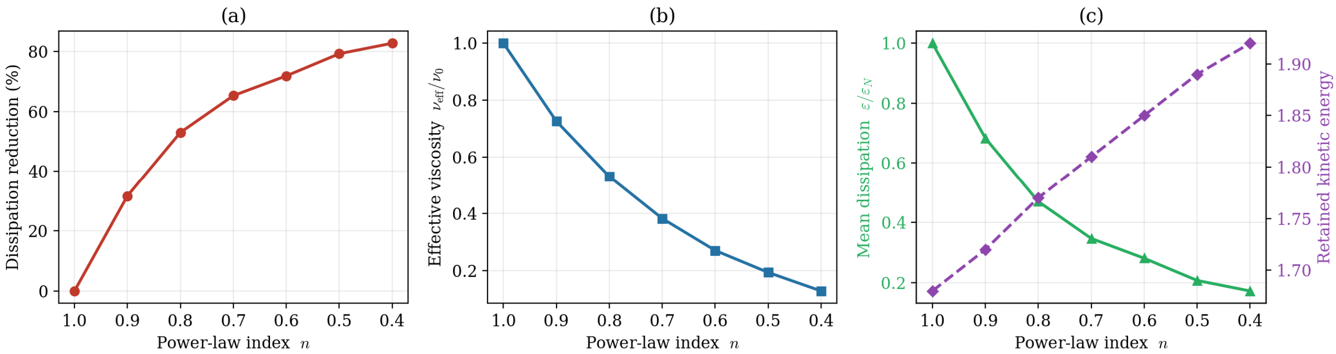

Fig. 9. Synthesis of the rheology sweep at fixed forcing ($k_f = 4$), relaxation time λ and zero-shear viscosity, $Re = 10^3$, over the power-law range $n = 1.0$ to 0.4 $(a = 2)$; all quantities nondimensional; (a) Dissipation-reduction metric (%) against power-law index, (b) Volume-averaged apparent viscosity ν_{eff}/ν_0, (c) Mean dissipation $\varepsilon/\varepsilon_N$ (green, left axis) and retained kinetic energy (purple, right axis).

The equation emphasises that DR here denotes this dissipation-reduction ratio, a bulk energetic measure internal to the two-dimensional model, and not an engineering wall-friction drag reduction. The angle brackets denote a space and time average in the statistically steady state. Table 2 and Fig. 9 summarise the results, which are properties of the two-dimensional model and are reported as comparative trends rather than quantitative predictions for three-dimensional flow. As n decreases the effective viscosity falls to as little as 13 per cent of its zero-shear value, the steady dissipation drops, and the retained kinetic energy rises correspondingly. The dissipation-reduction metric decreases monotonically, reaching approximately 83 per cent at n = 0.4.

The marginal gain per 0.1 decrement in n falls from 31.7 percentage points in the first step to 3.5 in the last, so the effect saturates as the fluid approaches the deep power-law regime: once the apparent viscosity in the active high-strain regions is already small, further reduction of n removes progressively less dissipation. This metric is a comparative measure of steady dissipation at fixed energy input, not a wall skin-friction coefficient, and the large percentages reflect the strong reduction of apparent viscosity in this idealised periodic setting rather than a quantitative prediction for wall-bounded flow, where the friction depends on the near-wall balance and on the viscosity-scale used to define the Reynolds number [6, 8]. The monotonic trend and its mechanism are robust, internally consistent across seven independent runs, and in qualitative agreement with the weakening of turbulence reported in three-dimensional DNS [6, 9].

6. Discussion

6.1. The mechanism across the three configurations

The three configurations are connected by a common response to the shear-dependent viscosity. That the apparent viscosity is depressed where the strain is strongest is a direct property of the constitutive law rather than a new finding; what is not evident from the law alone is how this local reduction reorganises the flow differently in each regime, and in particular how it acts on the vorticity and the dissipation in opposite directions. In the laminar channel this concentrates the velocity gradient near the wall and flattens the core (Figs. 3 (a), 3(b)). In the transitional layer it acts most strongly in the high-strain braids, lowering the peak strain that feeds the inflectional instability and so reducing both the growth rate and the saturation level of the disturbance, an effect that widens with Reynolds number (Fig. 5(b)). In developed turbulence the same strain-gating has a dual consequence that Fig. 8 makes plain: it sharpens the vorticity, allowing energy to reach smaller scales, while simultaneously smoothing the dissipation, because the viscosity that converts strain into dissipation is itself suppressed where the strain is largest. The central and least obvious of these consequences is the dissipation-limiting: because the dissipation density is $\varepsilon = \nu(\dot\gamma)\dot\gamma^2$ and the viscosity is suppressed exactly where $\dot\gamma$ is largest, the same rheology that sharpens the vorticity simultaneously caps the dissipation peaks, so that the vorticity becomes finer while the dissipation becomes smoother. This decoupling of the vorticity and dissipation structure, rather than the local viscosity reduction itself, is the main physical result of this study. This interpretation aligns with the structural picture from three-dimensional wall-bounded DNS. Arosemena et al. [8] reported that shear-thinning quasi-streamwise vortices grow, lift from the wall and weaken, all signatures of a disrupted near-wall self-sustaining cycle, while Karahan et al. [9] found that shear-thinning weakens turbulence and increases anisotropy, with the dominant effects confined to the high-shear inner layer.

6.2. Relation to viscoelastic and elasto-inertial turbulence

It is instructive to place the inelastic mechanism against the active body of work on viscoelastic turbulence, where elasticity rather than shear-thinning is the controlling ingredient. Elasto-inertial turbulence, now the subject of a dedicated review [17], is an intrinsically two-dimensional chaotic state sustained by polymer stretching, and recent simulations have mapped its transition routes, multistability and coherent structures [18-20]. Two-dimensional studies have proven central to that field: Lewy and Kerswell [21] showed that a centre-mode instability drives the transition in two-dimensional viscoelastic Kolmogorov flow, the same forced configuration used in section 5.2 [22], and Cheng et al. [23] analysed the anomalous Reynolds stress in two-dimensional elasto-inertial channel turbulence. A cautionary lesson from this literature is directly relevant to our numerics: Beneitez et al. [24] and Couchman et al. [25] demonstrated that polymer-stress diffusion, whether added explicitly or introduced implicitly by a dissipative scheme, can trigger a spurious polymer diffusive instability. Our inelastic model carries no conformation tensor and therefore no such reservoir, which removes that failure mode entirely, but the episode underscores the value of the exact Newtonian-limit recovery documented in section 3.1.3.

The distinction also clarifies the scope of our drag result. In dilute polymer solutions the dominant drag-reduction mechanism is elastic [26, 27], and purely inelastic shear-thinning contributes comparatively little net drag reduction in wall units once the Reynolds number is defined consistently [6, 8]. Our large dissipation-based percentages are therefore not in tension with that conclusion: they measure steady dissipation at fixed forcing in a periodic domain, a comparative diagnostic of the inelastic mechanism in isolation. This is a further reason to interpret the present dissipation-reduction metric as a model-internal energetic diagnostic rather than a predictor of engineering drag reduction.

6.3. Consequences of the two-dimensional idealisation

The computations are two-dimensional and doubly periodic, and this is the most important limitation of the study. Two-dimensional and three-dimensional turbulence differ fundamentally in their cascade dynamics: two-dimensional turbulence is governed by a dual cascade, with an inverse transfer of energy to large scales and a direct enstrophy cascade producing a k^{-3} spectral range [10], whereas three-dimensional turbulence has a direct energy cascade with a $k^{-5/3}$ inertial range and a genuinely dissipative small-scale structure. Because the dissipation and the drag are tied to this cascade structure, conclusions about turbulent dissipation and the drag metric drawn from the present model must be regarded as specific to two dimensions and are not claimed to hold quantitatively in three dimensions. Quantitative measures such as the precise spectral slope and the magnitude of the dissipation-reduction metric should therefore be read as properties of the model rather than transferable predictions. The trends, the suppression of disturbance growth, the sharpening of small scales and the monotonic decrease of dissipation with the power-law index, are mechanistic and are expected to persist in three dimensions, as the cited wall-bounded DNS support [7-9]. It is reassuring that two-dimensional models have repeatedly captured the essential physics of complex-fluid turbulence: the elasto-inertial turbulence literature cited above operates predominantly in two dimensions [17, 21, 23].

6.4. Limitations and future work

Several limitations bound the present conclusions. First, the free shear layer is inviscidly unstable, so the appropriate diagnostic is the amplification of disturbances rather than a critical Reynolds number; a linearly stable wall-bounded base flow would be required to define a genuine threshold [16, 28]. Second, the forced-turbulence statistics, although sampled over a window far longer than the large-eddy turnover time, exhibit a slow large-scale drift characteristic of the two-dimensional inverse cascade, so the higher moments would be tightened by ensemble realisations. Third, the model is purely inelastic; viscoelastic mechanisms are outside its scope. Fourth, the infinite-shear plateau μ_∞ was held negligible; a finite plateau, representative of real fluids, would regularise the centreline and is a straightforward extension. These point to the natural programme of future work: a wall-bounded influence-matrix formulation, three-dimensional computation, ensemble averaging, and the eventual addition of a conformation-tensor field [29, 30].

7. Conclusions

A verified pseudo-spectral framework has been used to study the influence of Carreau–Yasuda shear-thinning on transition and turbulence in an inelastic generalised Newtonian fluid. The findings reported here are numerical observations from an idealised two-dimensional model; they are presented as evidence for specific mechanisms rather than as general laws of shear-thinning turbulence. The principal findings are as follows:

- The solver reproduces the laminar Poiseuille flow and friction factor, the exact Ostwald–de Waele power-law profile and the decaying Taylor–Green vortex to relative errors between 10^{-14} and 10^{-7}, with the variable-viscosity diffusion term recovering the Newtonian operator exactly.
- In a perturbed free shear layer, shear-thinning suppresses the amplification of perturbation kinetic energy by one to three orders of magnitude, reducing both the linear growth rate and the saturation level, with the suppression strengthening at higher Reynolds number.
- Shear-thinning sharpens the small-scale vorticity, raising the high-wavenumber energy fraction by a factor of about 2.6 and the mean enstrophy by about eighteen per cent, while simultaneously rendering the dissipation field markedly less intermittent, because the constitutive law suppresses viscosity exactly where strain is largest.
- A dissipation-reduction metric decreases monotonically with the power-law index, reaching about 83 per cent at $n = 0.4$, with diminishing marginal returns.

Taken together, these results show that the defining feature of shear-thinning turbulence in this setting is not simply that viscosity falls at high strain, which the constitutive law guarantees, but that this reduction drives the vorticity and the dissipation in opposite directions, sharpening the former while smoothing the latter. The framework, exactly verifiable and inexpensive, provides a transparent basis for the wall-bounded, three-dimensional and viscoelastic extensions outlined above. Because the present results are obtained in a two-dimensional periodic model, whose cascade dynamics differ fundamentally from three-dimensional turbulence, the conclusions regarding turbulent dissipation and drag are presented as trends specific to this setting; their quantitative transfer to three-dimensional or wall-bounded flow remains to be established and is the natural object of the extensions noted above.

Author Contributions

A. Gad planned and initiated the project, developed the numerical method and software, performed the simulations and analysed the results, developed the mathematical modelling and verified the theory, and wrote, reviewed and approved the final version of the manuscript.

Acknowledgments

Not applicable.

Conflict of Interest

The author declared no potential conflicts of interest concerning the research, authorship, and publication of this article.

Funding

The author received no financial support for the research, authorship, and publication of this article.

Data Availability Statements

The solver and post-processing scripts that generate all results and figures are available from the author on reasonable request.

Declaration of Generative AI and AI-assisted Technologies in the Writing Process

During the preparation of this work the author used Claude (Anthropic) to assist with grammar correction and language polishing. After using this tool, the author reviewed and edited the content as needed and takes full responsibility for the content of the publication.

References

[1] Bird, R.B., Armstrong, R.C., Hassager, O., *Dynamics of Polymeric Liquids, Vol. 1: Fluid Mechanics*, 2nd ed., Wiley, New York, 1987.
[2] Poole, R.J., Inelastic and flow-type parameter models for non-Newtonian fluids, *Journal of Non-Newtonian Fluid Mechanics*, 320, 2023, 105106.
[3] Rudman, M., Blackburn, H.M., Graham, L.J.W., Pullum, L., Turbulent pipe flow of shear-thinning fluids, *Journal of Non-Newtonian Fluid Mechanics*, 118, 2004, 33–48.
[4] Rudman, M., Blackburn, H.M., Direct numerical simulation of turbulent non-Newtonian flow using a spectral element method, *Applied Mathematical Modelling*, 30, 2006, 1229–1248.
[5] Singh, J., Rudman, M., Blackburn, H.M., Chryss, A., Pullum, L., Graham, L.J.W., The importance of rheology characterization in predicting turbulent pipe flow of generalized Newtonian fluids, *Journal of Non-Newtonian Fluid Mechanics*, 232, 2016, 11–21.
[6] Singh, J., Rudman, M., Blackburn, H.M., The influence of shear-dependent rheology on turbulent pipe flow, *Journal of Fluid Mechanics*, 822, 2017, 848–879.
[7] Arosemena, A.A., Andersson, H.I., Solsvik, J., Turbulent channel flow of generalized Newtonian fluids at a low Reynolds number, *Journal of Fluid Mechanics*, 908, 2021, A43.
[8] Arosemena, A.A., Andersson, R., Andersson, H.I., Solsvik, J., Effects of shear-thinning rheology on near-wall turbulent structures, *Journal of Fluid Mechanics*, 925, 2021, A37.
[9] Karahan, D.T., Ranjan, D., Aidun, C.K., Turbulent channel flow of generalized Newtonian fluids at $Re_\tau = 180$, *Journal of Non-Newtonian Fluid Mechanics*, 314, 2023, 105015.
[10] Kraichnan, R.H., Inertial ranges in two-dimensional turbulence, *Physics of Fluids*, 10, 1967, 1417–1423.
[11] Carreau, P.J., Rheological equations from molecular network theories, *Transactions of the Society of Rheology*, 16, 1972, 99–127.
[12] Yasuda, K., Armstrong, R.C., Cohen, R.E., Shear flow properties of concentrated solutions of linear and star branched polystyrenes, *Rheologica Acta*, 20, 1981, 163–178.
[13] Trefethen, L.N., *Spectral Methods in MATLAB*, SIAM, Philadelphia, 2000.
[14] Boyd, J.P., *Chebyshev and Fourier Spectral Methods*, 2nd ed., Dover, New York, 2001.
[15] Canuto, C., Hussaini, M.Y., Quarteroni, A., Zang, T.A., *Spectral Methods in Fluid Dynamics*, Springer, Berlin, 1988.
[16] Charles, A., Peixinho, J., Ribeiro, T., Azimi, S., Rocher, V., Baudez, J.C., Bahrani, S.A., Asymmetry and intermittency in the rheo-inertial transition to turbulence in pipe flow, *Physics of Fluids*, 36, 2024, 054120.
[17] Dubief, Y., Terrapon, V.E., Hof, B., Elasto-inertial turbulence, *Annual Review of Fluid Mechanics*, 55, 2023, 675–705.
[18] Beneitez, M., Page, J., Dubief, Y., Kerswell, R.R., Multistability of elasto-inertial two-dimensional channel flow, *Journal of Fluid Mechanics*, 981, 2024, A30.
[19] Beneitez, M., Page, J., Dubief, Y., Kerswell, R.R., Transition route to elastic and elasto-inertial turbulence in polymer channel flows, *Physical Review Fluids*, 9, 2024, 123302.
[20] Khalid, M., Chaudhary, I., Garg, P., Shankar, V., Subramanian, G., The centre-mode instability of viscoelastic plane Poiseuille flow, *Journal of Fluid Mechanics*, 915, 2021, A43.
[21] Lewy, T., Kerswell, R.R., Revisiting 2D viscoelastic Kolmogorov flow: a centre-mode-driven transition, *Journal of Fluid Mechanics*, 1007, 2025, A55.
[22] Boffetta, G., Celani, A., Mazzino, A., Puliafito, A., Vergassola, M., The viscoelastic Kolmogorov flow: eddy viscosity and linear stability, *Journal of Fluid Mechanics*, 523, 2005, 161–170.
[23] Cheng, H., Zhang, H., Zhang, W., Wang, S., Li, X., Li, Y., Li, F.C., Anomalous Reynolds stress and dynamic mechanisms in two-dimensional elasto-inertial turbulence of viscoelastic channel flow, *Journal of Fluid Mechanics*, 1018, 2025, A33.
[24] Beneitez, M., Mrini, S., Kerswell, R.R., Linear instability in planar viscoelastic Taylor–Couette flow with and without explicit polymer diffusion, *Journal of Non-Newtonian Fluid Mechanics*, 345, 2025, 105459.
[25] Couchman, M.M.P., Beneitez, M., Page, J., Kerswell, R.R., Inertial enhancement of the polymer diffusive instability, *Journal of Fluid Mechanics*, 981, 2024, A2.
[26] Steinberg, V., Elastic turbulence: an experimental view on inertialess random flow, *Annual Review of Fluid Mechanics*, 53, 2021, 27–58.
[27] Buza, G., Beneitez, M., Page, J., Kerswell, R.R., Finite-amplitude elastic waves in viscoelastic channel flow from large to zero Reynolds number, *Journal of Fluid Mechanics*, 951, 2022, A3.
[28] Lopez-Carranza, S.N., Jenny, M., Nouar, C., Pipe flow of shear-thinning fluids, *Comptes Rendus Mecanique*, 340, 2012, 602–618.
[29] Mitishita, R.S., MacKenzie, J.A., Elfring, G.J., Frigaard, I.A., Fully turbulent flows of viscoplastic fluids in a rectangular duct, *Journal of Non-Newtonian Fluid Mechanics*, 293, 2021, 104570.
[30] Pope, S.B., *Turbulent Flows*, Cambridge University Press, Cambridge, 2000.
[31] Jalali, A., Amiri Delouei, A., Khorashadizadeh, M., Golmohammadi, A.M., Karimnejad, S., Mesoscopic Simulation of Forced Convective Heat Transfer of Carreau-Yasuda Fluid Flow over an Inclined Square: Temperature-Dependent Viscosity, *Journal of Applied and Computational Mechanics*, 6(2), 2020, 307–319.

Appendix A

For completeness and reproducibility, the central routines of the solver are listed below in abridged Python (NumPy) form. They correspond to the methods described in Section 3: the Chebyshev laminar solver (Listing A.1), the construction of the Fourier operators and velocity recovery (Listing A.2), the variable-viscosity diffusion term in stress-divergence form (Listing A.3, the implementation of Algorithm 1), and the assembly of the forced right-hand side (Listing A.4). The complete solver, the post-processing scripts and the figure-generation code are available as stated in the Data Availability statement.

```
def solve_cy_laminar(N, G, mu0, mu_inf, lam, n, a, relax=0.5, tol=1e-12):
    D, y = chebyshev_diff_matrix(N)      # collocation operator
    u = (G / (2*mu0)) * (1 - y**2)       # Newtonian initial guess
    for it in range(max_iter):
        gdot = D @ u                     # local shear rate du/dy
        mu   = carreau_yasuda(gdot, mu0, mu_inf, lam, n, a)
        L    = D @ (np.diag(mu) @ D)     # d/dy ( mu  d/dy )
        L[0, :], L[-1, :] = 0, 0         # impose no-slip rows
        L[0, 0], L[-1, -1] = 1, 1
        rhs = -G * np.ones(N + 1); rhs[0] = rhs[-1] = 0
        u_new = np.linalg.solve(L, rhs)
        u = (1 - relax) * u + relax * u_new   # under-relaxed update
        if norm(u_new - u) < tol:
            break
    return y, u, mu
```

Listing A.1. Picard iteration for the Carreau–Yasuda laminar channel profile.

```
class Spectral2D:
    def __init__(self, N, L, nu0):
        k1 = np.fft.fftfreq(N, d=L / N) * 2 * np.pi
        k2 = np.fft.rfftfreq(N, d=L / N) * 2 * np.pi
        self.kx, self.ky = np.meshgrid(k1, k2, indexing="ij")
        self.k2 = self.kx**2 + self.ky**2
        self.k2inv = np.where(self.k2 == 0, 0.0, 1.0 / self.k2)
        kmax = (2 / 3) * np.abs(k1).max()          # 2/3 de-aliasing cutoff
        self.mask = (abs(self.kx) <= kmax) & (abs(self.ky) <= kmax)

    def velocity(self, w_hat):                     # u = curl^-1 of vorticity
        psi = w_hat * self.k2inv                   # solve Poisson equation
        u = irfft2( 1j * self.ky * psi)
        v = irfft2(-1j * self.kx * psi)
        return u, v
```

Listing A.2. Construction of the Fourier operators and the velocity recovery.

```
def viscous_curl(self, w_hat):
    if self.newtonian:
        return -self.nu0 * self.k2 * w_hat         # exact Newtonian limit
    u, v = self.velocity(w_hat)
    ux = irfft2(1j*self.kx*rfft2(u)); uy = irfft2(1j*self.ky*rfft2(u))
    vx = irfft2(1j*self.kx*rfft2(v)); vy = irfft2(1j*self.ky*rfft2(v))
    gdot = np.sqrt(2*ux**2 + 2*vy**2 + (uy + vx)**2)
    nu   = carreau_yasuda(gdot, self.nu0, self.nu_inf, self.lam, self.n)
    t11 = 2*nu*ux;  t22 = 2*nu*vy;  t12 = nu*(uy + vx)   # tau = 2 nu S
    fx = 1j*self.kx*rfft2(t11) + 1j*self.ky*rfft2(t12)   # div(tau)_x
    fy = 1j*self.kx*rfft2(t12) + 1j*self.ky*rfft2(t22)   # div(tau)_y
    return (1j*self.kx*fy - 1j*self.ky*fx) * self.mask   # curl, de-aliased
```

Listing A.3. Velocity-stress evaluation of the variable-viscosity diffusion term (implementation of Algorithm 1).

```
def rhs(self, w_hat):                              # forced, variable-nu
    adv = self.nonlinear(w_hat)                    # -(u.grad) w
    visc = self.viscous_curl(w_hat)                # variable-viscosity term
    drag = -self.drag * w_hat                      # large-scale sink
    return adv + visc + drag + self.F_hat          # steady forcing F_hat
```

Listing A.4. Right-hand side for the forced, statistically steady turbulence runs.

ORCID iD

Ashish Gad https://orcid.org/0009-0008-1107-9144

How to cite this article: Gad A. Shear-thinning Control of Transition and Turbulent Dissipation: A Generalised Newtonian Spectral Study, *J. Appl. Comput. Mech.*, xx(x), 2026, 1–12. https://doi.org/10.22055/jacm.2026.49533.6054